Microfluidic printed 3D bioactive scaffolds for postoperative treatment of gastric cancer

Jiante Li [a], Tianru Zhu [b], Yiwei Jiang [b], Qingfei Zhang [c,e,*], Yan Zu [c,**], Xian Shen [b,d,***]

[a] *Department of Anorectal Surgery, The Second Affiliated Hospital and Yuying Children's Hospital of Wenzhou Medical University, Wenzhou, 325027, China*
[b] *Department of Gastrointestinal Surgery, The Second Affiliated Hospital and Yuying Children's Hospital of Wenzhou Medical University, Wenzhou, 325027, China*
[c] *Wenzhou Institute, University of Chinese Academy of Sciences, Wenzhou, 325001, China*
[d] *Department of Gastrointestinal Surgery, The First Affiliated Hospital of Wenzhou Medical University, Wenzhou, 325035, China*
[e] *The Key Laboratory of Pediatric Hematology and Oncology Diseases of Wenzhou, The Second Affiliated Hospital and Yuying Children's Hospital of Wenzhou Medical University, Wenzhou, 325027, China*

ARTICLE INFO

ABSTRACT

Tumor recurrence and tissue regeneration are two major challenges in the postoperative treatment of cancer. Current research hotspots are focusing on developing novel scaffold materials that can simultaneously suppress tumor recurrence and promote tissue repair. Here, we propose a microfluidic 3D-printed methacrylate fish gelatin (F-GelMA@BBR) scaffold loaded with berberine (BBR) for the postoperative treatment of gastric cancer. The F-GelMA@BBR scaffold displayed a significant killing effect on gastric cancer MKN-45 cells in vitro and demonstrated excellent anti-recurrence efficiency in gastric cancer postoperative models. In vitro experiments have shown that F-GelMA@BBR exhibits significant cytotoxicity on gastric cancer cells while maintaining the cell viability of normal cells. The results of in vivo experiments show that F-GelMA@BBR can significantly suppress the tumor volume to 49.7 % of the control group. In addition, the scaffold has an ordered porous structure and good biocompatibility, which could support the attachment and proliferation of normal cells to promote tissue repair at the tumor resection site. These features indicated that such scaffold material is a promising candidate for postoperative tumor treatment in the practical application.

1. Introduction

Gastric cancer is the second ordinary tumor in the world and the third most common tumor in China, seriously threatening human health [1]. Surgery remains the best treatment strategy for gastric cancer [2,3]. Despite the gradual advancements in surgical techniques, tumor remnants and circulating tumor cells persist after surgery, significantly contributing to elevated recurrence rates, which represent a major factor in increased mortality [4–7]. Systemic chemotherapy is commonly used in clinical practice to address the recurrence and metastasis of cancer after surgical treatment [8,9]. Despite great progress, chemotherapy faces the problems of systemic toxicity and side effects [10,11]. Otherwise, the damage of normal tissue during surgery is refractory to self-healing, greatly affecting the patient's quality of life [12–14]. To

settle these restrictions, new drug-loading systems, such as films, hydrogels, and fibers, have been applied to improve the efficacy of chemotherapy and promote the growth of normal tissues [15–19]. Unfortunately, it is difficult to synchronize the chemotherapy and repair processes, which are often carried out individually, resulting in low efficiency and high cost. Moreover, the preparation of carriers using synthetic polymers typically involves intricate synthesis and the inclusion of supplementary additives. This can result in a protracted preparation process and potential toxicity issues [20,21]. In contrast, natural bio-derived materials offer the benefits of excellent biocompatibility and ease of application in biomedical scenarios [22,23]. Therefore, developing a multifunctional bio-derived implant material that can not only eradicate residual tumor cells but also promote the growth of normal tissue is still anticipated.

In this paper, we proposed a composite scaffold containing both animal- and plant-derived active components with required functions for the postoperative treatment of gastric cancer, as shown in Fig. 1. Berberine (BBR) is a natural ingredient from the Ranunculaceae family and is extracted from Coptis chinensis. It is frequently applied for gastrointestinal disorders and is well tolerated [24,25]. In recent years, multiple researches have shown that BBR can induce cell apoptosis and cell cycle arrest, stop the proliferation of cancer cells, and improve the sensitivity of tumors to chemotherapeutics [26–29]. Gelatin is a natural polymer hydrolyzed and degraded from collagen obtained from animals such as pigs or fish [30,31]. Gelatin can optimize degradation and drug delivery kinetics by adjusting parameters such as crosslinking density and isoelectric point, and has high permeability and high retention [30]. At the same time, its excellent biocompatibility, low immunogenicity, easy operation, and biodegradability expand its use [32]. Because of these characteristics, gelatin is suitable for modifying and synthesizing drug delivery carriers with multiple forms for cancer treatment. For example, the prodrug initiator and indocyanine green encapsulated by photopolymerized methacrylate gelatin (GelMA) hydrogel particles developed by Zhang et al. are used for synergistic chemotherapy, photothermal therapy, and photodynamic therapy for melanoma [33]. In addition, Zhang and colleagues proposed a photopolymerization three-dimensional (3D) scaffold based on GelMA-derived bioink [34]. These 3D scaffolds containing platinum drugs can effectively inhibit the growth of breast cancer 4T1 cells and induce new tissue regeneration

and repair. Ma et al. skillfully used GelMA as a substrate to coordinate the manufacture of porous hydrogel particles by simulating the process of silicon colloidal crystal replication. These particles are modified by P-glycoprotein antibodies, which gives them the ability to capture drug-resistant blood cancer cells [35]. Fish gelatin (F-Gel) as a typical animal-derived component, possesses numerous advantages, including excellent biocompatibility, low immunogenicity, and availability from diverse sources [36,37]. The F-Gel-based biomaterial scaffold could be suitable for postoperative normal cell growth and the following tissue repair. Therefore, it is of great significance to construct a composite scaffold by combining F-Gel and BBR for the postoperative treatment of gastric cancer.

Herein, we used a microfluidic 3D printing strategy to generate BBR-loaded photopolymerized F-GelMA scaffolds (F-GelMA@BBR) for gastric cancer postoperative treatment. Microfluidic technology with high precision and controllability provides a general method for processing the fluid in microchannels. It can prepare a variety of nano or micro materials for disease treatment, drug delivery, and tissue engineering. Compared with traditional methods for the preparation of nano-drug carriers, microfluidic technology has the advantages of controllable size and morphology, good repeatability, and high encapsulation efficiency. Besides, microfluidic technology enables the fabrication of simple or multi-component microfibers with exceptional precision and controllability [38–40]. In the past decades, 3D printing has caught great attention in tissue repair, oncology, and other medical
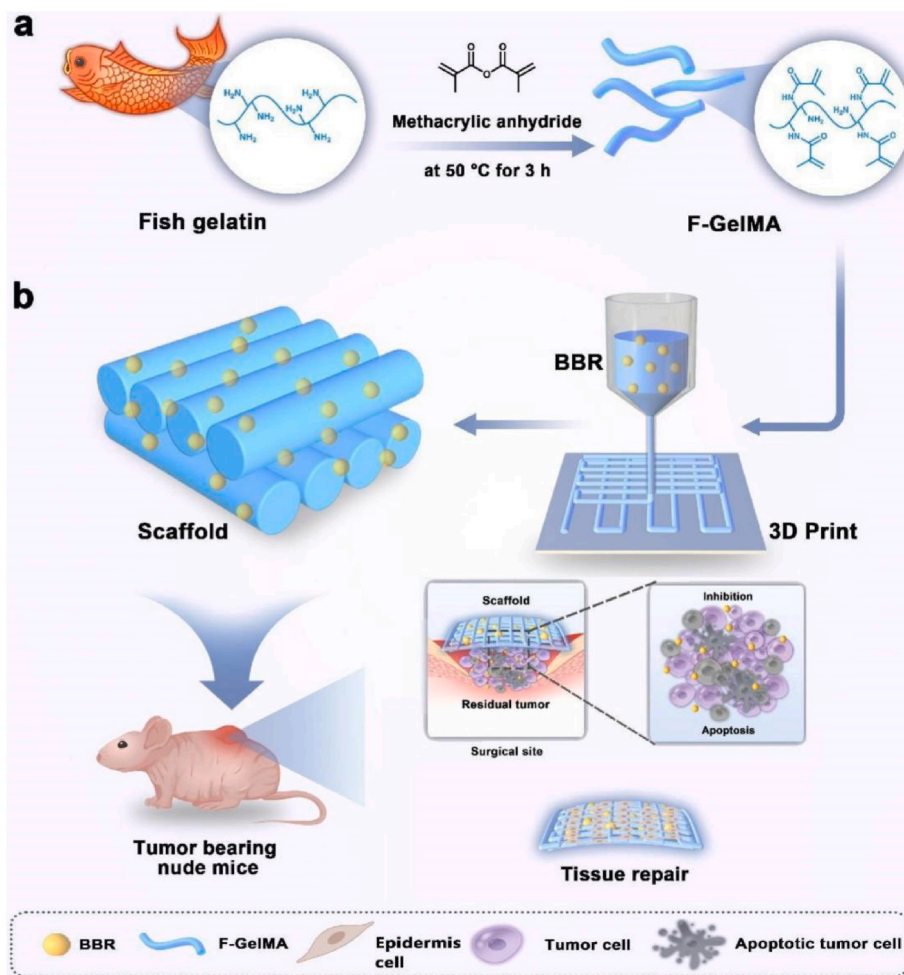
Fig. 1. Schematic instruction of the preparation processes of F-GelMA@BBR scaffolds by 3D printing and their application in postoperative treatment of gastric cancer. (a) Synthesis of methacrylate fish gelatin (F-GelMA) using fish gelatin (F-Gel) extracted from fish. (b) Subsequently, F-GelMA was mixed with berberine (BBR) to prepare F-GelMA@BBR scaffolds and implantation at the gastric cancer surgical site, residual cancer cells were effectively eradicated to prevent local tumor recurrence. In addition, F-GelMA@BBR could also serve as a culture platform for normal cell proliferation and tissue repair.

fields [41,42]. The multifunctional 3D structural scaffolds by 3D printing have been extensively studied in drug delivery, cell infiltration, nutrient supply, and tissue growth promotion [35,43,44]. Therefore, combining microfluidics and 3D printing technology offers a potential strategy for producing 3D structural scaffolds with high spatial and compositional precision [45–47]. Through the microfluidic 3D printing technology, the developed F-GelMA@BBR scaffolds demonstrated significant killing effects on gastric cancer MKN-45 cells in vitro and have significant inhibitory effects on local recurrence in gastric cancer postoperative models. In addition, the scaffold provides a porous structure and good biocompatibility and could provide the diffusion and proliferation of normal cells to promote the inward growth of new tissue at the tumor resection site. These charming features impart the F-GelMA@BBR scaffold with great potential in the practical usage of postoperative oncotherapy.

2. Experimental section

2.1. Materials

Fish gelatin (F-Gel), lithium phenyl-2,4,6-trimethylbenzoylphosphinate (LAP), and methacrylic anhydride were procured from Sigma-Aldrich. Berberine (BBR) and Calcein-AM/PI staining kit were offered from Dalian Meilun Bioscience Co. The Cell Counting Kit-8 was procured from Beyotime. The TUNEL apoptosis detection kit and anti-Ki-67 antibodies were generously supplied by ABCAM.

2.2. Synthesis of F-GelMA

The synthesis of methacrylate fish gelatin (F-GelMA) was according to the previous references with little modification [48,49]. In short, 20 g of F-Gel was dissolved in 200 mL ultrapure water containing 10 g of anhydrous sodium carbonate. After that, 4 mL of methacrylic anhydride was added and stirred at 50 °C for another 3 h. Maintaining the pH value at 8–9 through 10 % (w/v) sodium hydroxide. Subsequently, the solution underwent dialysis for 48 h to remove any remaining by-products. The final product was freeze-dried and preserved at 4 °C.

2.3. Microfluidic 3D printing of F-GelMA@BBR scaffold

For fabricating the scaffold, a pregel solution consisting of BBR (1 %, w/v) and F-GelMA (25 %, w/v) was prepared. Next, the pregel solution was pumped into a microfluidic device for printing. The flow rate was set to 3 mL h^{-1}, and the speed of the 3D printer was set to 5 mm s^{-1}. The printed F-GelMA@BBR scaffolds were solidified under UV light irradiation. By using the same conditions, the F-GelMA scaffolds without BBR were fabricated.

2.4. Characterizations

The stereomicroscope (Olympus BX51, Tokyo, Japan) was employed to observe the optical photographs of the scaffolds. The microstructure of the scaffolds was detected *via* scanning electron microscopy (SEM, Hitachi S3000 N, Japan) after dehydration by a series of 70 %, 80 %, 90 %, and 100 % ethanol.

2.5. Degradation and swelling experiment

The degradation behavior of the scaffolds was conducted by immersing the scaffolds in phosphate-buffered saline (PBS) containing type II collagenase 2 (2 U/mL). At indicated time intervals, the samples were collected and dried in a 60 °C oven until they reached a constant weight. The degradability of the samples was determined by measuring the extent of mass loss:

Residual weight [%] $= 100 \times W_D/W_I$,

In this equation, W_D and W_I stand for the weight of the dried scaffold before degradation and after degradation, respectively.

The swelling rate of the scaffolds was evaluated by immersing them in pure water at 25 °C. Within the scheduled time, excess water was removed by filter paper, and the wet weight of the scaffold was measured. The formula for calculating the swelling rate (SR) is shown below:

SR (%) $= (W_w - W_0)/W_0 \times 100\%$,

In this equation, W_0 and W_w represent the dry and wet weight of the scaffold, respectively.

2.6. In vitro drug release

The release behavior of the BBR-loaded F-GelMA scaffold was examined. To be brief, the F-GelMA@BBR scaffolds were immersed in 5 mL PBS, followed by a 168-h maintenance in a Gyratory shaker (150 rpm) at 37 °C. Then, 1 mL liquid was extracted and added with the same fresh medium after incubation for the suggested time point. Measuring the absorbance of the removal buffer at 334 nm using a microplate reader to construct the cumulative release curve.

2.7. In vitro biocompatibility study

Human gastric epithelial cells (HFE-145 cells) and mouse embryonal fibroblast cell (NIH-3T3) cells were selected to evaluate the in vitro biocompatibility of the scaffold with Dulbecco's Modified Eagle Medium. 2.5×10^5 cells/well were seed into a plate for 24 h and the cells were treated with PBS, F-GelMA scaffold (the concentration of F-GelMA is 15 % w/v), and F-GelMA scaffold (the concentration of F-GelMA is 25 % w/v), and incubated for 1, 2, and 3 days. After that, the CCK-8 assay was used to test the viability. Furthermore, the live and death of cells were evaluated using Calcein-AM and PI staining. Subsequently, the in vitro biocompatibility of the 3D scaffolds was evaluated by culturing with the HFE-145 cells and NIH-3T3. Two types of cells (2.5×10^5 cells/ well) were inoculated on the scaffolds for two days. Then, the cells were stained with Calcein-AM and observed under a fluorescence microscope.

2.8. In vitro cytotoxicity assay of F-GelMA@BBR scaffold

MKN-45 (a kind of human gastric cancer cells) were seeded into a 12-well plate and cultured for 12 h (2.5×10^5 cells/well). Next, the cells were treated with normal culture medium, F-GelMA scaffold alone, and F-GelMA@BBR scaffolds containing 30 μg/mL or 60 μg/mL BBR, and further incubated for 48 h. Live/dead staining, CCK-8 assay, and Annexin V/PI apoptosis detection were employed to study the cytotoxicity of drug-loaded scaffolds on tumor cells. Cells in each well were stained with Calcein-AM/PI and visualized. The cells were added with a CCK-8 kit and hatched for 2 h before using a microplate reader for the measurement of CCK-8. The apoptosis of cells was determined by flow cytometry after the co-staining with Annexin V and PI.

2.9. Cell migration and invasion assay

The ability of migration and invasion of tumor cells was detected. The treatment groups were the same as in the previous text. 2×10^4 cells in 1640 medium without serum were plated into the upper chamber of Corning Transwell Inserts. Next, after placing the upper chambers on the 24-well plate, 1640 complete medium was added to fill the bottom. 1 % crystal violet solution was used to stain the cells after incubation for 24. The cells in six random regions were counted to determine the number of migratory cells. The invasion assay was performed in the same protocol, and covered with matrigel at the chamber membrane.

2.10. In vivo antitumor efficacy on the MKN-45 tumor model

BALB/C-nude mice (6–8 weeks old) were bought from SPF (Beijing) Biotechnology Co., Ltd. 1×10^6 of MKN-45 cells were subcutaneous inoculated into the nude mice. These tumors were allowed to grow to a size of approximately 150 mm^3. Afterward, 70 % of the tumors were surgically removed. The mice were then randomly divided into four groups (n = 5), including the PBS group, F-GelMA scaffold, free BBR (50 mg/kg), and F-GelMA@BBR (containing 50 mg/kg of BBR). Tumor volume and body weight of the mice were recorded after the treatment every 2 days. All mice were euthanized humanely on the 21st day after treatment, and the main organs and tumors were collected. After fixation with paraformaldehyde, dehydration with alcohol, and embedding in paraffin, the samples were cut into 5 μm-wide sections. Then, immunohistochemical analysis including H&E, TUNEL, P53, PCNA, and Ki-67, was performed.

2.11. Specimen collection and sequencing

Tumors were collected from 4 groups. For the next generation RNA sequencing (RNA-seq), TRIzol®Reagents (Invitrogen; Termo Fisher Scientific, Inc., Inc., Waltham, MA, USA) were employed for collecting total RNA from tumors in the DNase environment. The weekly expression analysis was investigated by the Bioconductor Package DESeq2 (v1.26.0), and the statistical significance between the group of control and treatment group was determined using the P-value adjusted by the error detection rate <0.05 and the log 2-fold change (FC) > 2.0.

2.12. Gene enrichment analyses

Differential gene clustering map and differential gene volcano map were generated for the analysis of differentially expressed genes using the heatmap package and ggplot2 package. The differential gene Venn diagram shows the number of unique differential genes between samples or combinations, and it was generated using the Venn diagram package. Differential gene ontology (GO) enrichment histogram and differential Kyoto Encyclopedia of Genes and Genomes (KEGG) enrichment analyses were conducted to identify the signal transduction pathways associated with differentially expressed genes, using the cluster profiler package.

2.13. Statistical analysis

In vivo antitumor experiments were replicated five times (n = 5), while all other experiments were replicated three times (n = 3) unless otherwise specified. After the quantitative data were analyzed using Origin statistical software, the results were shown as the mean ± standard deviation. Differences were considered at P < 0.05.

3. Results and discussion

In this experiment, F-Gel was used to prepare F-GelMA, and then the 3D scaffold was printed by photo-crosslinking the mixture of F-GelMA and BBR (Fig. S1). As shown in Fig. 2a, the F-GelMA@BBR scaffold had a good organization and a regular 3D structure. A SEM was used to characterize the structure of the scaffold. According to Fig. 2b, a porous structure could be discovered on the scaffold. Good swelling and degradation behaviors are essential for an ideal drug microcarrier. To measure the swelling rate, the F-GelMA@BBR scaffold was immersed in PBS and the weight of the scaffold was detected for different time intervals. The results showed that the scaffold achieved equilibrium swelling within 1 h, resulting in a weight increase of approximately 500 % (Fig. 2c). The degradation behavior of F-GelMA@BBR was also investigated. The prepared F-GelMA@BBR scaffolds degraded about 90 % in 9 days (Fig. 2d). The gradual degradation of the scaffolds enables them to provide temporary support for tissue regeneration. To investigate the drug release behavior of F-GelMA@BBR, we conducted experiments on F-GelMA loaded with BBR. The content of BBR was detected by a microplate reader. The drug release curve of F-GelMA@BBR reaches equilibrium at about 48 h with a final release rate of approximately 58 % (Fig. 2e). The release of the drugs helps to kill the postoperative residual tumor cells.

The biocompatibility of the scaffold was verified through co-culture with HFE-145 cells and NIH-3T3 cells. The experimental group was treated with a drug-free F-GelMA scaffold with an F-GelMA concentration of 15 % or 25 %, while the control group was treated with the medium. The results of the live and dead staining showed that nearly no dead cells could be observed after different treatments for different time intervals (Fig. 3a and Fig. S2). Besides, the CCK-8 assay served as a quantitative analysis of the cell viability, and the results indicated that
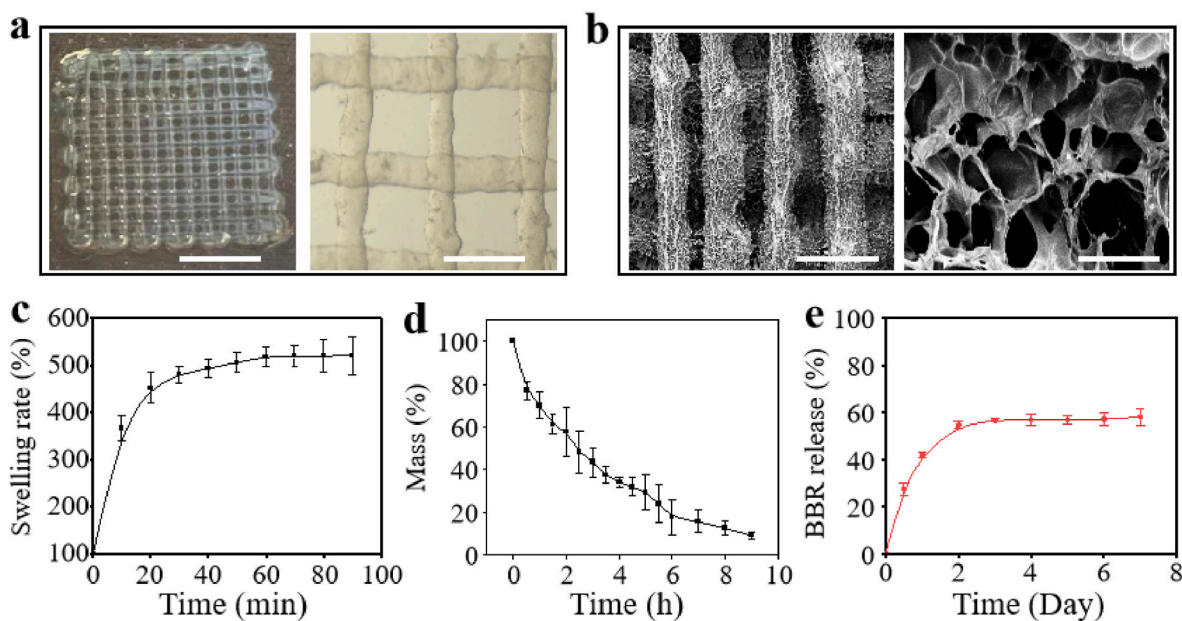

Fig. 2. Characterization of the F-GelMA@BBR scaffold. (a) Optical microscope images of the scaffold. Scale bars are 5 mm (left image) and 1 mm (right image). (b) SEM images of the scaffold. Scale bars are 1000 μm (left image) and 100 μm (right image). (c) Swelling rate of the scaffold. (d) Degradation behavior of the scaffold. (e) BBR release profiles of the scaffold in PBS.
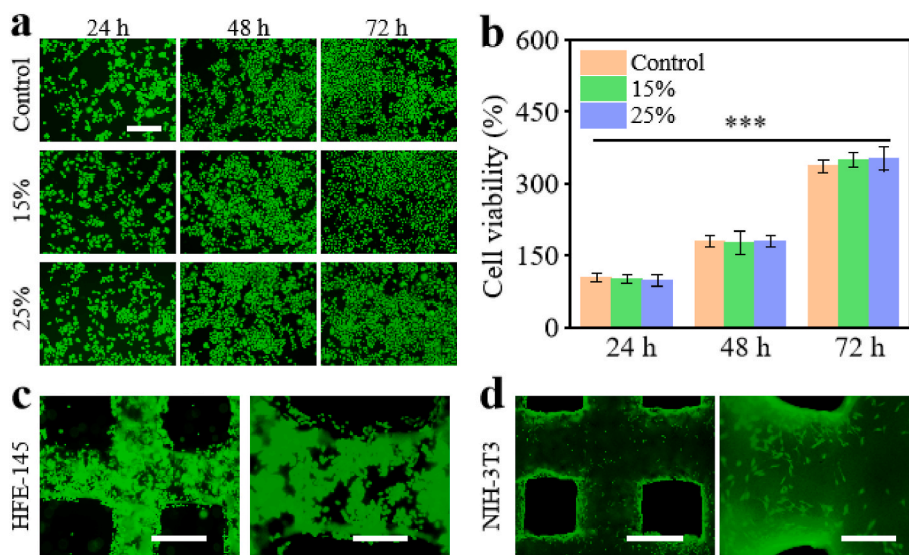
Fig. 3. In vitro biocompatibility of the scaffold. (a) Live/dead staining of HFE cells incubated with F-GelMA scaffolds with different concentrations for different time intervals. The scale bar is 250 μm. (b) Cell viability of HFE cells incubated with F-GelMA scaffolds with different concentrations for different time intervals by CCK8 assay. (c) Live/dead staining of HFE-145 cells after co-culture with F-GelMA scaffolds. The scale bars are 250 μm (left image) and 100 μm (right image). (d) Live/dead staining of NIH-3T3 cells after co-culture with F-GelMA scaffolds. The scale bars are 250 μm (left image) and 100 μm (right image).

the cells normally proliferated after the incubation with F-GelMA scaffolds (Fig. 3b). For treating postoperative tumors, except antitumor, tissue repair is also important for the health of patients. Thus, we detected the in vitro biological activity of scaffolds through culture with HFE-145 and NIH-3T3. The experiments showed that the scaffold can support the attachment and promote the proliferation of normal cells effectively (Fig. 3c and d). These results may indicate the scaffolds have excellent biocompatibility and may act as a 3D culture platform for
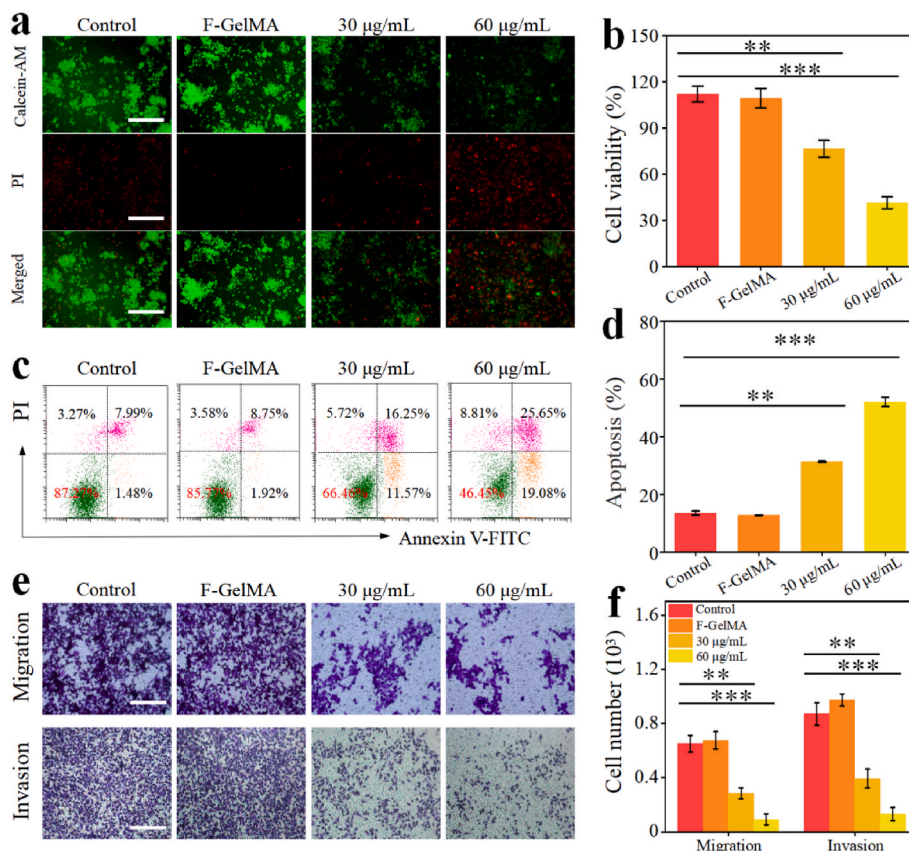
Fig. 4. In vitro anti-tumor evaluation of F-GelMA@BBR scaffold. (a) Live/dead staining of MKN-45 cells incubated with different scaffolds for 48 h. The scale bar is 200 μm. (b) Cell viability of MKN-45 cells incubated with different scaffolds for 48 h by CCK8 assay. (c) Representative flow cytometry data and corresponding statistic data of the apoptosis rate of MKN-45 cells incubated with different scaffolds for 48 h. (e, f) Migration and invasion evaluation (e) and the corresponding quantitative analysis (f) of MKN-45 cells incubated with different scaffolds for 48 h. The scale bars are 250 μm.

facilitating tissue repair.

To explore the cytotoxicity of F-GelMA@BBR, the MKN-45 cell line (a poorly differentiated signet ring cell carcinoma) was selected. MKN-45 cells were cocultured with F-GelMA@BBR scaffolds, and the results of confocal microscopy and flow cytometry showed that the cells effectively internalized the BBR released from the scaffold (Fig. S3, S4). After exploring the IC_{50} of BBR (Fig. S5), in vitro anti-tumor experiments were divided into the control group, F-GelMA scaffold group, F-GelMA@BBR (loading 30 μg/mL of BBR), and F-GelMA@BBR (loading 60 μg/mL of BBR). According to the live-dead staining analysis, few tumor cells died in the control and F-GelMA groups. However, F-GelMA@BBR carries 30 or 60 μg/mL BBR could obviously kill tumor cells, and a large number of dead cells were observed (Fig. 4a). Besides, the quantitative analysis data of the relative cell activity of co-cultured cells in each group had a consistent trend with live/dead staining results (Fig. 4b). Similar cell-killing effects of F-GelMA@BBR could also be observed against human gastric cancer cells (MGC-803) cells (Fig. S6). Quantitative analysis of MKN-45 cells by flow cytometry showed that the rates of apoptosis of the control group and the F-GelMA scaffold group were 13.46 % and 12.76 %, respectively, greatly lower than that in the F-GelMA@BBR treatment group. The cell apoptosis rates of F-GelMA@BBR (30 μg/mL) and F-GelMA@BBR (60 μg/mL) treatment groups were 31.25 % and 52.06 %, respectively (Fig. 4c and d). Besides, Transwell tests were performed to determine whether BBR could restrain the metastasis and invasion of tumor cells. The results showed that the drug-containing groups exhibited significantly lower numbers of invasive and migrating cells compared to the two drug-free groups (Fig. 4e and f). These results indicated that the prepared F-GelMA@BBR scaffold had effective anti-cancer efficacy in vitro.

To further investigate the therapeutic efficacy of F-GelMA@BBR in vivo, a subcutaneous gastric tumor model in BALB/c nude mice was established. Specifically, MNK-45 gastric cancer cells were subcutaneously implanted in nude mice to mimic tumor formation. Seven days later, the tumor has burgeoned to approximately 150 mm³. Then, to simulate postoperative operation, 70 % of the tumor was surgically removed from the tumor-bearing nude mice before being treated with different scaffolds (Fig. 5a). The nude mice were randomly divided into PBS group, F-GelMA group, BBR group, and F-GelMA@BBR group. Particularly, the growth trend of the F-GelMA@BBR group was greatly inhibited and compared with other groups (Fig. 5b). According to Fig. 5c and d, the change curve in tumor volume better reflected the anti-tumor

effect of the scaffold. Also, the control group and the F-GelMA group had a consistent trend, and the treatment of BBR and F-GelMA@BBR could significantly inhibit tumor growth. After treatment for 21 days, tumor size was 583.0 mm³ in the control group and 399.2 mm³ in the BBR group, while the size was merely 289.0 mm³ in the F-GelMA@BBR group, indicating the effectiveness of BBR as a tumor growth inhibitor. The analysis indicated that the drug-loaded scaffolds had an effective killing effect on the long-term inhibition of tumors. Throughout this study period, we closely monitored the body weight. As demonstrated in Fig. 5e, the body weight in different groups all gradually increased. Besides, there was no major difference in the performance of the heart, liver, spleen, lung, and kidney with the normal morphology and structure (Fig. S7). The blood biochemical results showed no significant abnormalities in the four experimental groups (Fig. S8). These results revealed that F-GelMA@BBR exhibits potent tumor growth inhibition and a favorable safety profile.

To further assess the therapeutic effects of F-GelMA@BBR, we analyzed the pathological changes in specimens of tumors. H&E staining revealed the presence of tumor cells in all groups (Fig. 6a). The control group and the F-GelMA group had larger and denser tumor cells. In contrast, the tumor cell clusters were smaller and the necrotic tumor cells were more pronounced in the F-GelMA@BBR group and the direct BBR administration group. In addition, TUNEL staining was applied to evaluate the percentage of apoptotic cells in each group (Fig. 6a and b). Similarly, the TUNEL staining results showed that the F-GelMA@BBR group had the highest apoptotic rate of tumor cells (99.66 %), while the values of the control, F-GelMA, and BBR treatment groups were 14.12 %, 13.68 %, and 76.56 %, respectively. Proliferation-associated nuclear antigen (Ki67) is a marker of tumor proliferation and is highly related to tumor progression. The study revealed that both the F-GelMA@BBR group and the group administered with BBR directly displayed reduced Ki67 expression compared to the group of control and F-GelMA (Fig. 6a and b). The F-GelMA@BBR group demonstrated the lowest Ki67 expression in tumor tissues, with a positivity rate of about 8.59 %. P53 and PCNA were detected as indicators of tumor invasion (Fig. 6a and b). As expected, the F-GelMA@BBR treatment group showed the lowest level expression of p53 and PCNA, with positive rates of 4.9 % and 15.86 %, respectively (Fig. 6a and b). These outcomes confirmed that the drug-loaded F-GelMA@BBR scaffold could effectively kill gastric cancer cells and inhibit tumor growth.

Furthermore, RNA-seq analyses of tumor tissues were studied for the
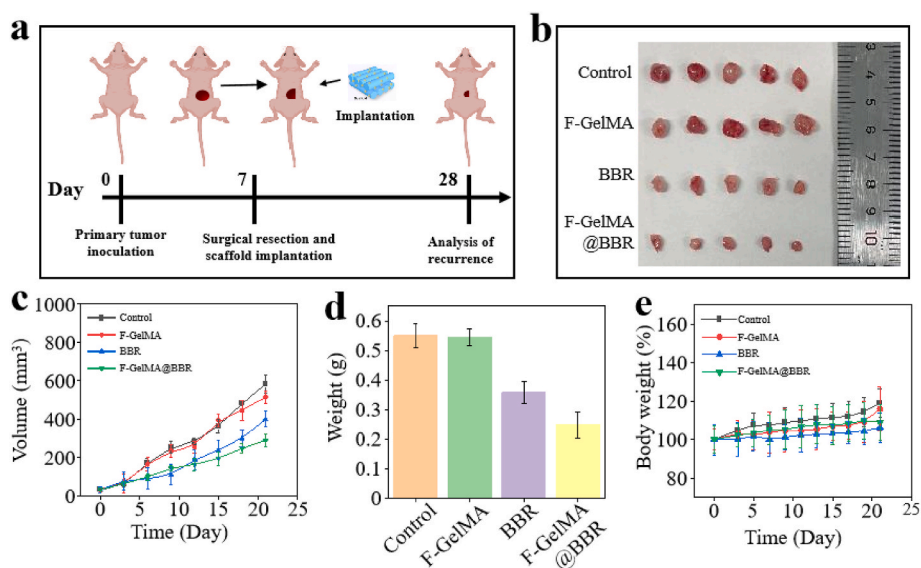
Fig. 5. In vivo anti-tumor ability of F-GelMA@BBR. (a) Schematic diagram of animal experiment processes. (b) Photos of tumors removed from mice at the end of treatment. (c) Tumor volume curves with different treatments. (d) Tumor weight after different treatments. (e) Body weight changes of mice with different treatments.
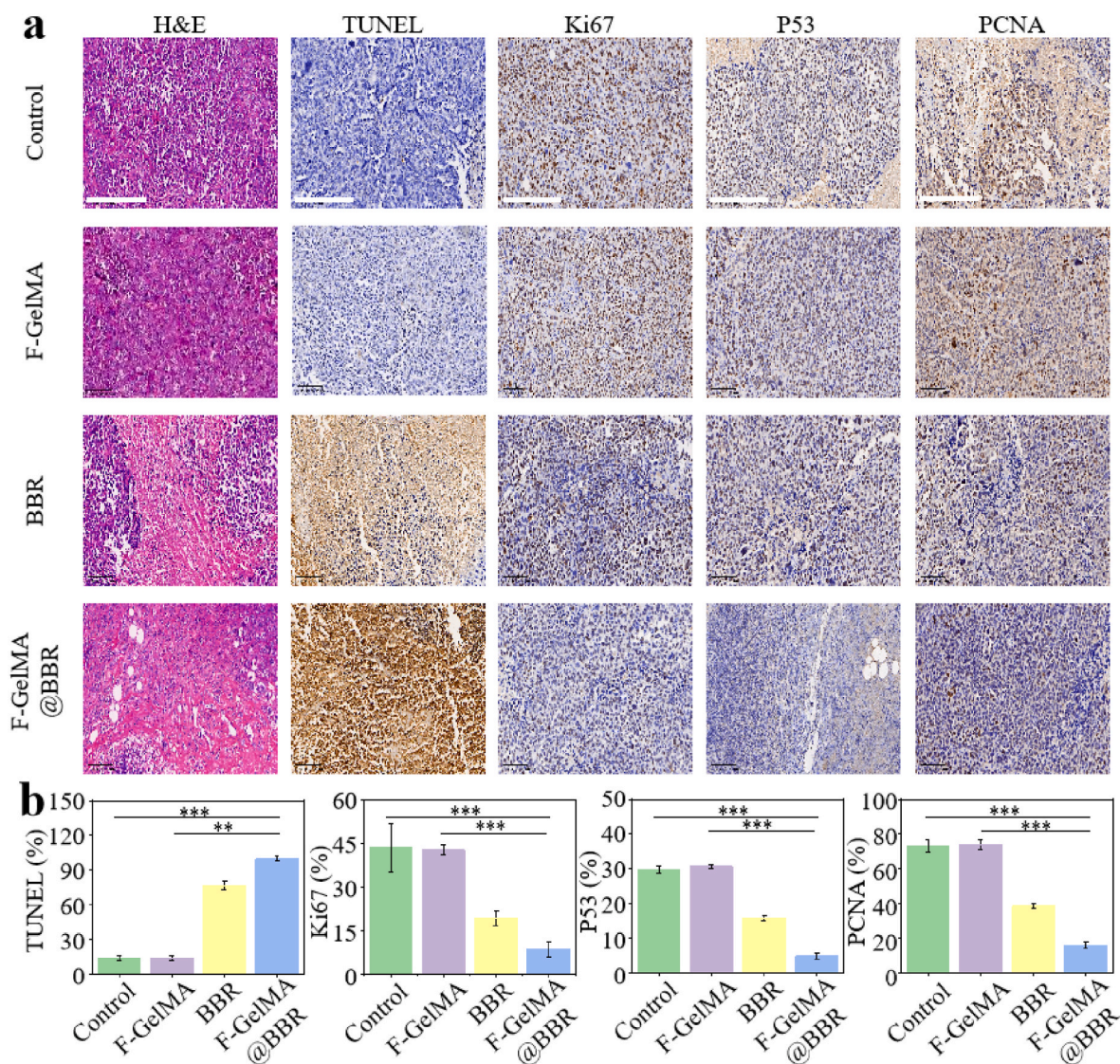
Fig. 6. The anti-tumor mechanisms of F-GelMA@BBR. (a) H&E, TUNEL, Ki67, P53, and PCNA staining of tumor tissues after different treatments. Scale bars are 200 μm. (b) The proportion of positive cells after TUNEL, Ki67, P53, and PCNA staining in each group.

potential mechanism of F-GelMA@BBR in inhibiting tumor proliferation and promoting apoptosis. As shown in Fig. S9, we assessed the quality of RNA-seq and found that the squares of the Pearson correlation coefficients (R^2) were all greater than 0.9, suggesting that the involved biological experiments were reproducible with little variation. It was found that F-GelMA@BBR treatment significantly changed the transcriptional map of tumor cells by comparing it with the control group (Fig. 7a). The volcanic map analysis displayed that compared with the control group, 141 and 142 of the RNAs of tumor cells in the F-GelMA@BBR treatment group were greatly down-regulated and upregulated (Fig. 7b), respectively, which indicated that those genes are potentially key genes in suppressing tumor proliferation and progression. Next, we performed the KEGG and GO analyses (Fig. 7c and d), and the results found that the F-GelMA@BBR treatment group mainly functions through cytokine activation, extracellular space, and inflammatory response, and may regulate the apoptosis and necrosis of tumor cells through IL-17 signal pathway, nucleotide-binding oligomerization domain (NOD)-like receptor signal pathway, and other pathways. In addition, 324 abnormally expressed genes were found in the F-GelMA@BBR group through the Venn diagram (Fig. 7e), suggesting that these genes are potential key genes. The directed acyclic graph revealed the biological process of enrichment of differentially expressed genes

(Fig. 7f). Meanwhile, the sequencing results of the F-GelMA group displayed no great variation compared with the control group (Fig. S10). Also, BBR treatment changed the transcriptional map (Fig. S11, S12). Overall, F-GelMA@BBR treatment significantly changed the transcriptional map of tumor cells and inhibited tumor proliferation and apoptosis through many pathways like the IL-17 signal pathway, NOD-like receptor signal pathway, etc.

4. Conclusion

In summary, this research presents a new method for postoperative gastric cancer treatment and tissue repair using F-Gel-based hydrogel scaffolds loaded with BBR through microfluidic 3D printing. The study demonstrated that the BBR-loaded F-GelMA@BBR could efficiently kill gastric cancer cells in vitro and greatly inhibit the development of postoperative residual tumors in vivo. The tumor volume of the experimental group was only 49.7 % of the control group at the end of the 21-day experiment. This emphasizes that F-GelMA@BBR with 3D structure, shows superior therapeutic effect and effectiveness. Besides, the hydrogel scaffold has favorable biocompatibility and suitable size, providing flexible spaces for supporting normal cell attachment, spreading, and proliferation in vitro and facilitating tissue ingrowth for
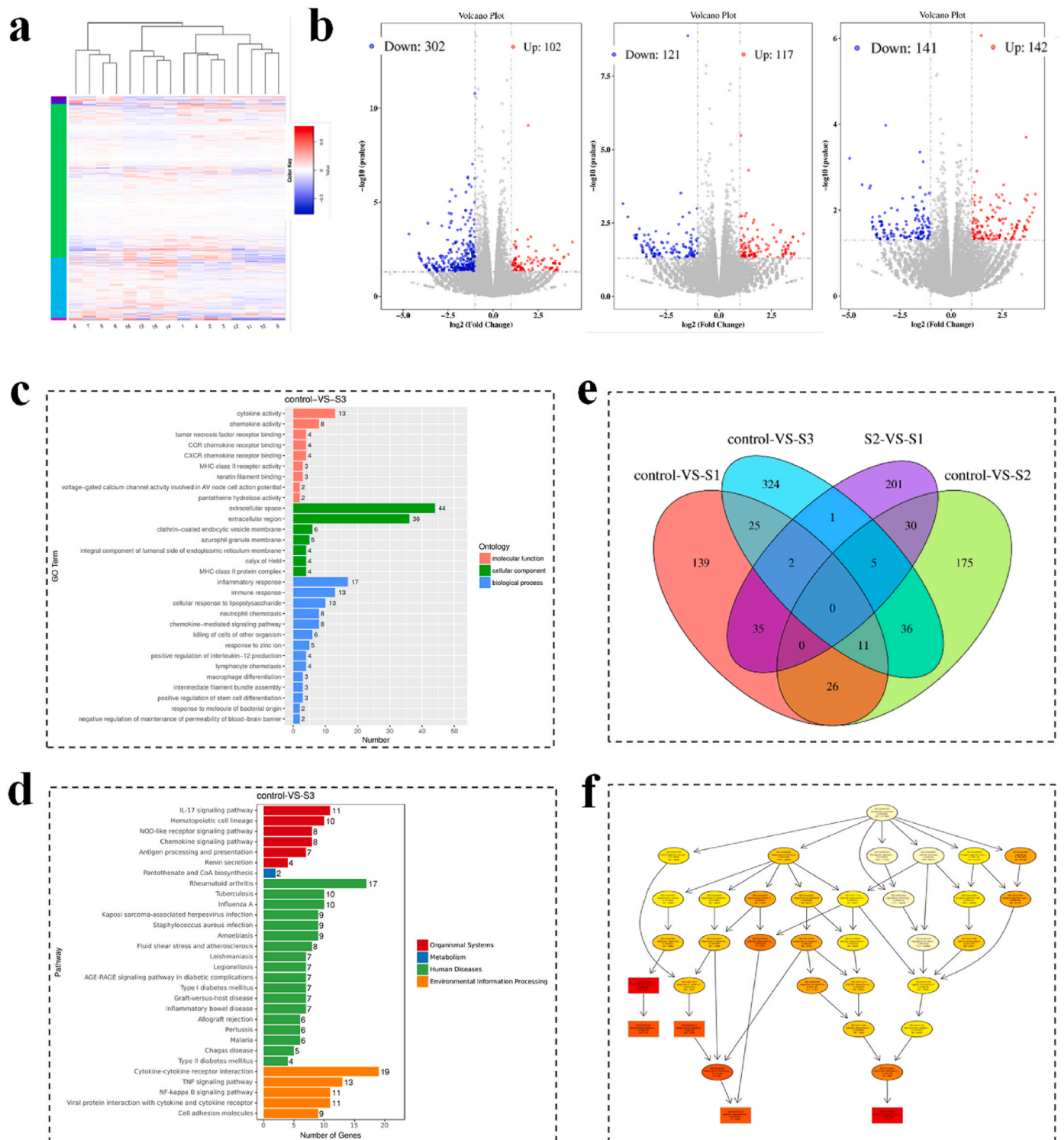
Fig. 7. RNA-seq and differential gene expression analyses. (a) Heatmap showing the relative expression of differentially expressed genes in different groups. (b) Volcano plots showing differentially expressed genes for all groups. Blue dots signify low expression and red dots signify high expression. (c) GO enrichment histogram revealed the biological process, cellular components, and molecular functions of differentially expressed genes involved in F-GelMA@BBR suppression of tumors. (d) KEGG pathway clustering revealed the pathway of F-GelMA@BBR suppression of tumors. (e) Venn diagram showed the differentially expressed genes among all groups. (f) The directed acyclic graph revealed the biological process of enrichment of differentially expressed genes between the control group and the F-GelMA@BBR group.

tissue regeneration after surgery. Hence, the drug-loaded scaffold displayed satisfactory therapeutic effects in improving postoperative gastric cancer treatment. Overall, the F-GelMA@BBR system exhibits tremendous potential as a versatile drug delivery system for cancer

therapy in clinical applications. However, our research does have some limitations. First of all, whether it can maintain a good therapeutic effect after orthotopic implantation in nude mice remains to be studied. Secondly, the pharmacokinetics of drugs in vivo is worthy of further

exploration. These problems need to be solved through more extensive and long-term research.

CRediT authorship contribution statement

Yan Zu: Conceptualization, Supervision, Writing – review & editing. Xian Shen: Conceptualization, Funding acquisition, Resources, Supervision. Tianru Zhu: Methodology, Validation, Writing – review & editing. Jiante Li: Data curation, Investigation, Methodology, Writing – review & editing. Qingfei Zhang: Conceptualization, Funding acquisition, Writing – review & editing. Yiwei Jiang: Writing – review & editing

Declaration of competing interest

The authors declare that they have no known competing financial interests or personal relationships that could have appeared to influence the work reported in this paper.

Data availability

Data will be made available on request.

Acknowledgements

Appendix A. Supplementary data

Supplementary data to this article can be found online at https://doi.org/10.1016/j.mtbio.2023.100911.

References

[1] R.L. Siegel, K.D. Miller, H.E. Fuchs, A. Jemal, Cancer statistics, 2022, CA- Cancer J. Clin. 72 (1) (2022) 7–33.

[2] F. Chemi, D.G. Rothwell, N. McGranahan, S. Gulati, C. Abbosh, S.P. Pearce, C. Zhou, G.A. Wilson, M. Jamal-Hanjani, N. Birkbak, J. Pierce, C.S. Kim, S. Ferdous, D.J. Burt, D. Slane-Tan, F. Gomes, D. Moore, R. Shah, M. Al Bakir, C. Hiley, S. Veeriah, Y. Summers, P. Crosbie, S. Ward, B. Mesquita, M. Dynowski, D. Biswas, J. Tugwood, F. Blackhall, C. Miller, A. Hackshaw, G. Brady, C. Swanton, C. Dive, Pulmonary venous circulating tumor cell dissemination before tumor resection and disease relapse, Nat. Med. 25 (10) (2019) 1534–1539.

[3] K. Takahashi, T. Yoshikawa, S. Morita, T. Kinoshita, M. Yura, S. Otsuki, M. Tokunaga, Y. Yamagata, A. Kaito, H. Katai, Different risks of nodal metastasis by tumor location in remnant gastric cancer after curative gastrectomy for gastric cancer, Gastric Cancer 23 (1) (2019) 195–201.

[4] Y. Ishiguro, H. Sakihama, T. Yoshida, N. Ichikawa, S. Homma, M. Fukai, H. Kawamura, N. Takahashi, A. Taketomi, Prognostic significance of circulating tumor cells with mesenchymal phenotypes in patients with gastric cancer: a prospective study, Ann. Surg Oncol. 28 (2) (2020) 1178–1186.

[5] Z. Wang, L. Luo, Y. Cheng, G. He, B. Peng, Y. Gao, Z.-s. Jiang, M. Pan, Correlation between postoperative early recurrence of hepatocellular carcinoma and mesenchymal circulating tumor cells in peripheral blood, J. Gastrointest. Surg. 22 (4) (2017) 633–639.

[6] P.A.J. Crosbie, R. Shah, P. Krysiak, C. Zhou, K. Morris, J. Tugwood, R. Booton, F. Blackhall, C. Dive, Circulating tumor cells detected in the tumor-draining pulmonary vein are associated with disease recurrence after surgical resection of NSCLC, J. Thorac. Oncol. 11 (10) (2016) 1793–1797.

[7] H. Ito, J. Sato, Y. Tsujino, N. Yamaguchi, S. Kimura, K. Gohda, K. Murakami, M. Onimaru, T. Ohmori, F. Ishikawa, H. Inoue, Long-term prognostic impact of circulating tumour cells in gastric cancer patients, World J. Gastroenterol. 22 (46) (2016) 10232–10241.

[8] K. Nishibeppu, S. Komatsu, D. Ichikawa, T. Imamura, T. Kosuga, K. Okamoto, H. Konishi, A. Shiozaki, H. Fujiwara, E. Otsuji, Venous invasion as a risk factor for recurrence after gastrectomy followed by chemotherapy for stage III gastric cancer, BMC Cancer 18 (1) (2018), 108.

[9] D. Soto Veliz, K.L. Lin, C. Sahlgren, Organ-on-a-chip technologies for biomedical research and drug development: a focus on the vasculature, Smart Med. 2 (1) (2023), e20220030.

[10] I. Shaked, Matthew A. Oberhardt, N. Atias, R. Sharan, E. Ruppin, Metabolic network prediction of drug side effects, Cell. Syst. 2 (3) (2016) 209–213.

[11] D. Galeano, S. Li, M. Gerstein, A. Paccanaro, Predicting the frequencies of drug side effects, Nat. Commun. 11 (1) (2020) 4575.

[12] Q. Saiding, Z. Cai, L. Deng, W. Cui, Inflammation self-limiting electrospun fibrous tape via regional immunity for deep soft tissue repair, Small 18 (39) (2022), 2203265.

[13] Y. Zhuang, W. Cui, Biomaterial-based delivery of nucleic acids for tissue regeneration, Adv. Drug Deliv. Rev. 176 (2021), 113885.

[14] Z. Pang, Y. Li, A. Huang, X. Li, Y. Liu, Y. Meng, Effect of HCH nutrition management combined with early exercise nursing on nutrition status and postoperative rehabilitation of patients after gastric cancer surgery, Evid-Based Compl. Alt. Med. 9 (2023), 9792489.

[15] W. Chen, K. Shi, J. Liu, P. Yang, R. Han, M. Pan, L. Yuan, C. Fang, Y. Yu, Z. Qian, Sustained co-delivery of 5-fluorouracil and cis-platinum via biodegradable thermo-sensitive hydrogel for intraoperative synergistic combination chemotherapy of gastric cancer, Bioact. Mater. 23 (2023) 1–15.

[16] H. Zhang, Y. Liu, G. Chen, H. Wang, C. Chen, M. Li, P. Lu, Y. Zhao, Immunotherapeutic silk inverse opal particles for post-surgical tumor treatment, Sci. Bull. 65 (5) (2020) 380–388.

[17] G. Kuang, Q. Zhang, Y. Yu, L. Shang, Y. Zhao, Cryo-shocked cancer cell microgels for tumor postoperative combination immunotherapy and tissue regeneration, Bioact. Mater. 28 (2023) 326–336.

[18] X. Ding, Y. Yu, W. Li, Y. Zhao, In situ 3D-bioprinting MoS2 accelerated gelling hydrogel scaffold for promoting chronic diabetic wound healing, Matter 6 (3) (2023) 1000–1014.

[19] X. Zhang, G. Chen, X. Fu, Y. Wang, Y. Zhao, Magneto-Responsive microneedle robots for intestinal macromolecule delivery, Adv. Mater. 33 (44) (2021), e2104932.

[20] M. Alsehli, Polymeric nanocarriers as stimuli-responsive systems for targeted tumor (cancer) therapy: recent advances in drug delivery, Saudi Pharmaceut. J. 28 (3) (2020) 255–265.

[21] N.H. Abd Ellah, S.A. Abouelmagd, Surface functionalization of polymeric nanoparticles for tumor drug delivery: approaches and challenges, Expert Opin. Drug Deliv. 14 (2) (2016) 201–214.

[22] K. Qian, H. Qian, J. Cai, W. Yue, X. Yu, B. Liu, Evaluation of cisplatin-hydrogel for improving localized antitumor efficacy in gastric cancer, Pathol. Res. Pract. 215 (4) (2019) 755–760.

[23] R. Laurano, M. Boffito, G. Ciardelli, V. Chiono, Wound dressing products: a translational investigation from the bench to the market, Eng. Regen. 3 (2) (2022) 182–200.

[24] C. Hou, H. Liang, Z. Hao, D. Zhao, Berberine ameliorates the neurological dysfunction of the gastric fundus by promoting calcium channels dependent release of ACh in STZ-induced diabetic rats, Saudi Pharmaceut. J. 31 (3) (2023) 433–443.

[25] Y. Tong, X. Zhao, R. Wang, R. Li, W. Zou, Y. Zhao, Therapeutic effect of berberine on chronic atrophic gastritis based on plasma and urine metabolisms, Eur. J. Pharmacol. 908 (2021), e174335.

[26] H. Du, J. Gu, Q. Peng, X. Wang, L. Liu, X. Shu, Q. He, Y. Tan, M.S. Hasnain, Berberine suppresses EMT in liver and gastric carcinoma cells through combination with TGFβR regulating TGF-β/smad pathway, Oxid. Med. Cell. Longev. 2021 (2021) 1–21.

[27] L. He, Z. Zhong, M. Chen, Q. Liang, Y. Wang, W. Tan, Current advances in coptidis rhizoma for gastrointestinal and other cancers, Front. Pharmacol. 12 (2022) 775084.

[28] M. Wang, L. Sun, L. Wang, Y. Sun, J. Chen, Effects of berberine on circular RNA expression profiles in human gastric cancer cells, Evid-Based Compl. Alt. Med. 2021 (2021) 1–16.

[29] J. Xu, Y. Long, L. Ni, X. Yuan, N. Yu, R. Wu, J. Tao, Y. Zhang, Anticancer effect of berberine based on experimental animal models of various cancers: a systematic review and meta-analysis, BMC Cancer 19 (1) (2019) 589.

[30] J. Alipal, N.A.S. Mohd Pu'ad, T.C. Lee, N.H.M. Nayan, N. Sahari, H. Basri, M. I. Idris, H.Z. Abdullah, A review of gelatin: properties, sources, process, applications, and commercialisation, Mater. Today: Proc. 42 (2021) 240–250.

[31] Z. Dong, X. Meng, W. Yang, J. Zhang, P. Sun, H. Zhang, X. Fang, D.-A. Wang, C. Fan, Progress of gelatin-based microspheres (GMSs) as delivery vehicles of drug and cell, Mater. Sci. Eng. C 122 (2021) 111949.

[32] M. Santoro, A.M. Tatara, A.G. Mikos, Gelatin carriers for drug and cell delivery in tissue engineering, J. Contr. Release 190 (2014) 210–218.

[33] Q. Zhang, X. Wang, G. Kuang, Y. Zhao, Pt(IV) prodrug initiated microparticles from microfluidics for tumor chemo-, photothermal and photodynamic combination therapy, Bioact. Mater. 24 (2023) 185–196.

[34] Q. Zhang, X. Wang, G. Kuang, Y. Yu, Y. Zhao, Photopolymerized 3D printing scaffolds with Pt(IV) prodrug initiator for postsurgical tumor treatment, Research 2022 (2022), 9784501.

[35] X. Ma, Z. Zhao, H. Wang, Y. Liu, Y. Xu, J. Zhang, B. Chen, L. Li, Y. Zhao, P-Glycoprotein antibody decorated porous hydrogel particles for capture and release of drug-resistant tumor cells, Adv. Healthcare Mater. 8 (13) (2019), e1900136.

[36] M.G. Kang, M.Y. Lee, J.M. Cha, J.K. Lee, S.C. Lee, J. Kim, Y.-S. Hwang, H. Bae, Nanogels derived from fish gelatin: application to drug delivery system, Mar. Drugs 17 (4) (2019) 246.

[37] X. Zhang, G. Kim, M. Kang, J. Lee, J. Seo, J. Do, K. Hong, J. Cha, S. Shin, H. Bae, Marine biomaterial-based bioinks for generating 3D printed tissue constructs, Mar. Drugs 16 (12) (2018) 484.

[38] X. Zhao, Z. Chen, Y. Liu, Q. Huang, H. Zhang, W. Ji, J. Ren, J. Li, Y. Zhao, Silk fibroin microparticles with hollow mesoporous silica nanocarriers encapsulation for abdominal wall repair, Adv. Healthcare Mater. 7 (21) (2018), 1801005.

[39] J. Shen, M. Ma, M. Shafiq, H. Yu, Z. Lan, H. Chen, Microfluidics-assisted engineering of pH/enzyme dual-activatable ZIF@polymer nanosystem for Co-delivery of proteins and chemotherapeutics with enhanced deep-tumor penetration, Angew. Chem., Int. Ed. Engl. 61 (14) (2022), e202113703.

[40] J. Shen, M. Shafiq, M. Ma, H. Chen, Synthesis and surface engineering of inorganic nanomaterials based on microfluidic technology, Nanomaterials 10 (6) (2020) 1177.

[41] D. Fan, Y. Li, X. Wang, T. Zhu, Q. Wang, H. Cai, W. Li, Y. Tian, Z. Liu, Progressive 3D printing technology and its application in medical materials, Front. Pharmacol. 11 (2020) 122.

[42] M. Tatullo, B. Marrelli, C. Benincasa, E. Aiello, I. Makeeva, B. Zavan, A. Ballini, D. De Vito, G. Spagnuolo, Organoids in translational oncology, J. Clin. Med. 9 (9) (2020) 2774.

[43] X. Wang, Y. Yu, C. Yang, C. Shao, K. Shi, L. Shang, F. Ye, Y. Zhao, Microfluidic 3D printing responsive scaffolds with biomimetic enrichment channels for bone regeneration, Adv. Funct. Mater. 31 (40) (2021), 2105190.

[44] L. Yang, L. Fan, X. Lin, Y. Yu, Y. Zhao, Pearl powder hybrid bioactive scaffolds from microfluidic 3D printing for bone regeneration, Adv. Sci. (2023), e2304190.

[45] X. Ding, Y. Yu, L. Shang, Y. Zhao, Histidine-triggered GO hybrid hydrogels for microfluidic 3D printing, ACS Nano 16 (11) (2022) 19533–19542.

[46] G. Gonzalez, I. Roppolo, C.F. Pirri, A. Chiappone, Current and emerging trends in polymeric 3D printed microfluidic devices, Addit. Manuf. 55 (2022), 102867.

[47] S. Mi, Z. Du, Y. Xu, W. Sun, The crossing and integration between microfluidic technology and 3D printing for organ-on-chips, J. Mater. Chem. B 6 (39) (2018) 6191–6206.

[48] A.G. Kurian, R.K. Singh, K.D. Patel, J.-H. Lee, H.-W. Kim, Multifunctional GelMA platforms with nanomaterials for advanced tissue therapeutics, Bioact. Mater. 8 (2022) 267–295.

[49] K. Yue, G. Trujillo-de Santiago, M.M. Alvarez, A. Tamayol, N. Annabi, A. Khademhosseini, Synthesis, properties, and biomedical applications of gelatin methacryloyl (GelMA) hydrogels, Biomaterials 73 (2015) 254–271.